NDT&E International 74 (2015) 58–65

Contents lists available at ScienceDirect

NDT&E International

journal homepage: www.elsevier.com/locate/ndteint

Weld defect detection using PPM EMAT generated shear horizontal ultrasound

P.A. Petcher *, S. Dixon **

Department of Physics, University of Warwick, Coventry CV4 7AL, UK

ARTICLE INFO

Article history:
Received 20 February 2015
Received in revised form
16 May 2015
Accepted 18 May 2015
Available online 27 May 2015

Keywords:
Shear horizontal (SH)
PPM EMAT
Defect detection
Welds

ABSTRACT

Austenitic welds are inspected using PPM EMAT generated shear horizontal (SH) waves. Results are compared to measurements taken using a 1D piezoelectric phased array using the total focusing method (TFM). For the first time there is clear experimental evidence of the SH wave method demonstrating higher sensitivity to defect detection. SH waves suffer less beam steering in a weld than either compression or SV waves, which can miss defects due to weld microstructure anisotropy and attenuation. All defects were identified from every side of the weld/plate using the SH waves, but this was not possible using the piezoelectric transducer.

1. Introduction

The welding process has the potential to introduce many different defects into a component [1], and as a consequence, weld inspection is a major application of non-destructive testing (NDT). Welded areas can be difficult to inspect, due to the access challenges caused by the presence of a weld cap, and in austenitic welds particularly, the highly anisotropic and attenuating nature of the weld region. There are added complications arising from the heat-affected zone (HAZ), and the many different forms that weld defects can take. This work describes a method of using shear horizontal (SH) ultrasound waves, generated and detected by periodic permanent magnet (PPM) electromagnetic acoustic transducers (EMATs), to detect and laterally size defects within a stainless steel plate weld. This method will be compared to the performance of a piezoelectric phased array operating in full matrix capture (FMC) mode, with signals processed using the total focusing method (TFM).

1.1. Weld defects

Cracking can occur during and after the welding process. For example, if there has been insufficient weld liquid flow, or if there are high strains on the solidifying weld pool, solidification/hot cracking can occur. Fusion welding between two similar metals creates a heat-affected zone (HAZ), which has its material properties changed (relative to the parent material) during the weld without being melted itself [1]. After the weld has been completed, residual stresses between the base material and the weld (the molten weld contracting always causes residual stresses [1]), combined with hydrogen diffusing into the HAZ, can lead to hydrogen induced HAZ cold cracking. Other defects that can occur during fusion welding include the formation of porosity or cavities due to gas or shrinkage (into which gas can diffuse), solid inclusions (such as non-metallic slag, flux, and oxides, as well as metallic copper and tungsten), lack of fusion (the weld bead adheres poorly to the base metal), incomplete penetration (the weld bead does not reach the root of the weld region), and imperfect shape such as an undercut [2–4]. A welded component subjected to fatigue loads can develop fatigue cracks in joints, which will subsequently propagate under further loading [1].

Ultrasound has been used extensively for the inspection of welds. Time of flight diffraction (TOFD) is an ultrasound technique developed for the NDT of nuclear power plants [5–7], and it has been used for general weld inspection [4]. Standard inspections may use a normal incidence compression wave transducer to check the HAZ for laminar defects, followed by an angle incidence transducer for defects in the weld itself (requiring a reflection, or skip, off the back-wall, before reaching the weld region). The use of several different transducers, covering a range of incident angles, may be required to detect some defects, and there are variations on this method that use phased arrays, allowing the incident angle to be easily changed. As well as conventional piezoelectric transducer systems, the use of EMATs for weld inspection has also been considered. EMATs producing compression or shear vertical (SV) waves can have insufficient sensitivity to detect the very low amplitude signals scattered by weld defects, and this has led to the

* Principal corresponding author.
** Corresponding author. Tel.: +44 2476573877; fax: +44 2476573133.
E-mail addresses: P.A.Petcher@warwick.ac.uk (P.A. Petcher), S.M.Dixon@warwick.ac.uk (S. Dixon).

http://dx.doi.org/10.1016/j.ndteint.2015.05.005

creation of hybrid laser-EMAT systems for ultrasonic weld inspection [8,9]. However, this approach does not overcome issues with weld microstructure anisotropy.

Austenitic welds have a large oriented grain structure, and this causes an ultrasound beam to skew and be strongly attenuated (via scattering and absorption). The details of how the beams are skewed and attenuated are dependent on the sample (particularly the weld) and the inspection method used, but in general, SV ultrasound waves suffer from the effects of skew and attenuation to a greater extent than compression waves [10]. However, these issues are still present for compression waves, and there are additional problems such as mode-conversion from compression to SV waves.

1.2. Shear horizontal ultrasound waves

Shear horizontal (SH) ultrasound waves are guided waves (they have propagation properties affected by the geometry of the propagation medium), with symmetric and anti-symmetric modes; phase and group speeds are dependent on frequency, sample thickness, and the bulk shear wave speed [11,12]. The properties of the different modes can be very useful, such as in thickness measurement [13], but in this case they are a complication. SH0 has a thickness independent speed, equal to the shear wave speed, and is non-dispersive (the phase and group speed are equal to the shear wave speed for all frequencies). The oscillation direction of SH ultrasound is in the plane of the surface where the wave was generated, and perpendicular to the propagation direction, as shown in Fig. 1, with respect to a reference interface, which is typically a sample surface. Under certain conditions, such as over short propagation distances, SH waves can be treated as bulk waves.

Compared to compression or SV ultrasonic waves, SH waves polarised parallel to the direction of an austenitic weld will propagate through with less reflection, beam steering, and attenuation, and will not mode-convert upon interaction with a defect in the weld that extends parallel to the welding direction [14,10]. This potentially increased sensitivity to defects makes SH waves a good candidate for ultrasonically inspecting welds.

1.3. Periodic-permanent-magnet electromagnetic acoustic transducers

Periodic-permanent-magnet electromagnetic acoustic transducers (PPM EMATs) can be used to generate and detect SH ultrasound waves [15–17]. EMATs are extensively used in NDT, and their operating principles are well covered in the existing literature [18–25]. PPM EMATs have a series of permanent magnets with periodically alternating north and south (N/S) poles, which sets the primary wavelength of the ultrasound generated. A coil of

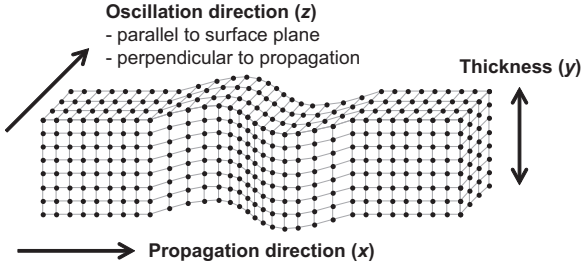

Fig. 1. A simple diagram of a SH ultrasound wave; the scale of the displacements is greatly exaggerated. Oscillation direction is parallel to the surface plane, and perpendicular to the propagation direction. As depicted here, the SH displacement is constant along the thickness direction, but this is only the case for the SH0 guided mode.

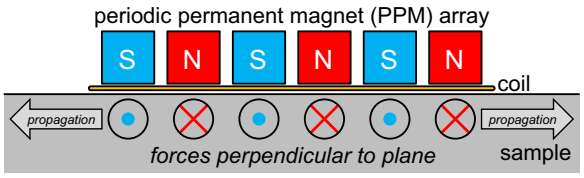

Fig. 2. Side view of a PPM EMAT for generation and detection of SH ultrasound waves. The magnets have alternating polarisation, and when a current is pulsed through the coil, periodic forces are generated in the conducting sample. The periodic magnet spacing sets the wavelength of the SH waves.

wire runs in the direction of the alternation, and when current is pulsed through the coil, eddy currents are created in the sample, that lead to a Lorentz force perpendicular to the wire direction and parallel to the surface plane [15,26,25,27], as shown in Fig. 2. These Lorentz forces generate the SH wave in the sample. For conditions under which the SH wave can be treated as a bulk wave, the propagation angle of a PPM EMAT can be varied by using the pulse frequency [28,29,27] (this cannot be done with SV waves as they do not satisfy the free-surface boundary conditions [15]), but this is not exploited in this work.

1.4. Weld inspection using PPM EMATs

The properties of SH waves make them suitable for weld inspection, but EMATs can suffer from a low signal-to-noise ratio (SNR), which favours piezoelectric transducers and hence compression waves. Relative to a metal like aluminium, steel has a lower electrical conductivity, higher density, and higher attenuation, all of which reduce EMAT efficiency [30], but with appropriate electronics and signal processing, this problem can be overcome. Investigations using SH waves on weld defects have previously used EMAT arrays [31–34] and PPM EMATs [31,35] and both have been shown to work successfully. PPM EMATs, compared to EMAT arrays, are easy to construct with a fundamental wavelength of choice, are simpler to drive (only a standard EMAT pulser is required, not a driver for an array), and only a single digitiser is required for detection, not an array. EMATs generally do not need to be profile matched, and can work on rough surfaces, but the alternating magnetic field of PPM EMATs does require close proximity to the sample surface. The maximum lift-off is dependent on the details of the sample (material and dimensions) and EMAT design, particularly the magnet width (2.5 mm magnet width for a 6 mm wavelength PPM EMAT for example), but less than 1 mm lift-off from the surface is advised, and within this study the EMATs were in contact with the sample.

1.5. Full matrix capture and the total focusing method

Full matrix capture (FMC) and the total focusing method (TFM) are used in this work as a comparison, and as such, they are briefly described here, and in detail within the literature [36].

FMC is simply the collection of time-domain data for all possible array element combinations within the phased array; the first array element is pulsed, and the scattered waves are recorded from all array elements and stored separately (pulse on element 1, receive on elements 1–64 if there are 64 elements). Next, the second array element is pulsed, and again, all array elements record the scattered waves (pulse on element 2, receive on elements 1–64). This is repeated by pulsing all remaining array elements in turn, and receiving on all array elements for each. The axes of the data matrix are then generation element, detection element, and time, with each data point representing an instantaneous amplitude [36].

TFM calculates the time taken for a wave to travel from each generating array element to each possible scatterer in the imaging region (the area the operator wishes to inspect), and then back to each detecting element. For this work, the total path must include the wedge attached to the phased array probe, including the refraction at the wedge/steel boundary. The speed in each region must be known for the times of flight to be calculated accurately. Each possible scatterer is then a focusing point, forming a rectangular array (dimensions of *X*-position and *Y*-position), with each element of the array representing the combined magnitude of the waves scattered from that point; this can be referred to as the image array. For each generation–detection pair, and each point in the image array, the analytic signal component (where the analytic signal is the real original signal combined with the Hilbert transform of the original signal [37]) at the time point representing the generation–scatterer–detection flight time is added to the image array. Using the analytic signal allows the TFM process to take advantage of the phase and magnitude of any received signals. All of these contributions are summed, and the magnitude taken of the result (simply the absolute value of each image element), to produce the final TFM image [36].

2. Sample with weld defects

The plate shown in Fig. 3, on which all the experiments were conducted, was provided by AMEC and manufactured by Sonaspection. The ultrasound compression speed was measured as 5740 ± 10 m/s using multiple back-wall reflections generated by a piezoelectric transducer. The ultrasound shear speed was measured as 3150 ± 10 m/s using SH waves generated by PPM EMATs; the separation of the EMATs was varied to get a relative measurement of distance versus time of flight. The plate allows for inspection of the defects from both sides of the weld and both sides of the plate. The sample documentation gives information on the defects within the weld, as listed in Table 1.

3. Inspection using SH PPM EMATs

Scans of the sample were taken using both 6 mm wavelength and 10 mm wavelength PPM EMATs (designed and produced at the University of Warwick). PPM EMATs with wavelengths smaller than 6 mm can be constructed, but as the wavelength becomes shorter, so must the size of the magnets used to produce the periodically alternating magnetic field; smaller magnets will generally result in a reduction in the SH wave generation and detection performance. If the wavelength is made much larger than 10 mm, the transducer can become relatively large and unwieldy. Some applications justify the usage of specific wavelengths, but if a technique can operate with standard wavelength PPM EMATs, it is certainly an advantage, and hence 6 mm and 10 mm are the initial wavelengths trialled.

As shown in Fig. 4, a separate generation (labelled "G") and detection (labelled "D") transducer was used, and two scan configurations were tested, in-line and side-by-side; the diagram designates the sides of the sample that are later used to label the results. Both in-line and side-by-side configurations were scanning for waves back-scattered from defects, and no configuration was attempted for the transmitted case.

The SH ultrasound is generated primarily within the skin depth of the sample below the generation EMAT. For a thin sample, an SH0 guided wave would be formed immediately, and for a very thick sample, the wave would propagate as a bulk wave. This sample is not thin, but it is not thick enough for the wave to be

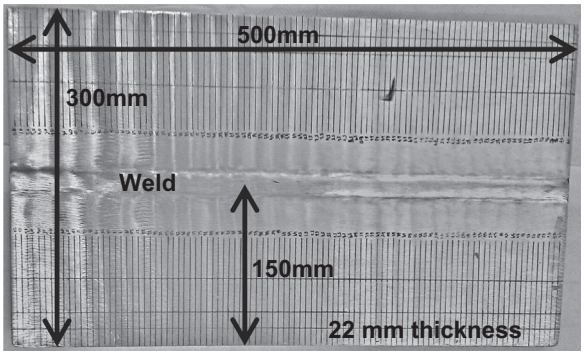

Fig. 3. The 316L stainless steel plate contains six defects within the double-V weld. The plate thickness is 25 mm at the weld cap (with some variation), and 22.3 ± 0.1 mm elsewhere, measured using callipers at the edges. Most of the error in the thickness is from actual variation in the thickness rather than due to difficulties with the measurement. The lines drawn on the sample are markers for the B-scan positions.

Table 1
The 316L stainless steel thick plate (Fig. 3) is documented as having the defects listed in this table. All of the defects are oriented longitudinally (in the direction of the weld), and have 0° of skew from that orientation. The defect tolerances are length ± 1 mm, height ± 1 mm, tilt/skew $\pm 5°$. The length is the distance the defect extends longitudinally (along the welding direction). The height is the extent of the defect through the weld (in the direction of the thickness of the plate). The depth is the distance from the weld surface that the defect starts at (note that even for a zero depth, the defect is not visible optically from the surface). The start position is how far the defect is from the "left" side of the plate. Tilt is the angle of the defect relative to the thickness direction (so a completely vertical defect has an angle of 0°.)

ID no.	Defect type	Length (mm)	Height (mm)	Depth (mm)	Start (mm)	Tilt (deg)
1	Centreline crack	35	6	0	35	0
2	Lack of side wall fusion	35	4	3	100	40
3	Side wall crack	45	5	2	180	35
4	Toe crack	40	4	0	260	35
5	Centreline crack	40	14	3	345	0
6	Lack of side wall fusion	50	3	3	415	35

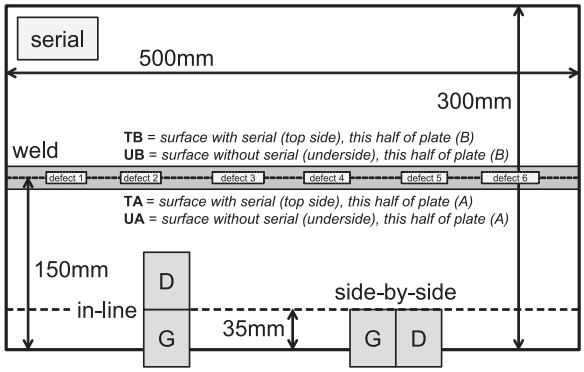

Fig. 4. There are two scan configurations for the thick stainless steel plate with a weld. Both configurations scan laterally across the sample (parallel to the weld), with the direction chosen so that for each side of the weld/plate, the scan starts at the same section of weld (the edge nearest defect 1). The scan progresses in 5 mm increments. For the in-line case, the lateral scan position relates to the lateral centre of the transducer pair. For the side-by-side case, the lateral scan position is the same as the line between the generator and detector (also the lateral centre of the transducer pair). "Serial" represents the position of the identification sticker for the sample; sides TA and TB are the same surface as the serial, whereas sides UA and UB are the opposite surface (such that the sticker is on the reverse surface to that being scanned). The defect lateral positions are indicated (but these are not accurate positions in terms of offset from the centreline of the weld).

considered a bulk wave. In addition, the frequency–thickness product leads to higher order modes being formed (potentially even higher than SH4), resulting in a complicated interference pattern, with the energy distribution varying in terms of depth and distance from the transducer. Although not the ideal uniform distribution of the SH0 mode, there should be sufficient energy at all depths to detect any defects present.

Back-scattered waves were favoured primarily for two reasons. Firstly, when it comes to detecting small defects, waves diffracting around the defect mean that detecting a scattered signal that was not previously present, without interfering signals at the same time of arrival obscuring the defect signal, is considerably easier than detecting a small change to a transmitted signal that is always present, but may have small amplitude variations due to, for example, variations in the wave generation efficiency. Secondly, the relatively small size of the sample means that reflections from the sides of the sample can easily interfere with the transmitted signal, resulting in small amplitude changes that could readily be mistaken for the presence of small defects. In contrast, if the back-scattered wave appears in a region of time that is usually devoid of other signals, a signal reflected from the side of the sample could easily be identified, as the behaviour of the arrival time of the wave during a B-scan would be very different compared to that of a defect. This does not mean that techniques considering the transmitted wave are of no value when using SH waves, but for this particular sample and technique, waves back-scattered from the defect are clearly favourable. For terms of keeping track of the starting point of the scan, the sample was split into four "sides" (TA, TB, UA, and UB), and these were recorded consistently over the various scans performed.

The SH PPM EMATs were controlled by a RITEC RPR-4000 pulser/receiver. The pulser was set to provide a 4 cycle current burst to the generation EMAT, at 330 kHz for a 10 mm wavelength EMAT, and at 550 kHz for a 6 mm wavelength EMAT. The RITEC RPR-4000 applied a band-pass filter to signals received from the detection EMAT, with cut-off points at 0.2 MHz and 2.5 MHz. The signals are then sent to a digitiser (a GaGe Octopus 8482 Express CompuScope within a computer) sampling at 25 MHz. At each scan position, the current pulse was applied 64 times (with a suitable repetition rate, so that the previous ultrasound waves had fully attenuated before the next pulse was sent), and the received data was averaged over the 64 collections; all averaging was performed after the data had been passed from the digitiser to the MATLAB control software on the computer.

The separation required between the EMATs and the weld region, to avoid the dead-time of the receiver covering the signal from the weld, meant that the EMATs had to be placed against the edge of the sample. Consequently, the signals that are inseparable from those from the weld region (generator to weld to detector) include those first reflecting off the back edge (generator to back edge to weld to detector) and those reflecting off the back edge after interacting with the weld (generator to weld to back edge to detector). However, as the back edge is relatively constant, it is not expected that these will cause any significant difficulty; they are expected to simply provide an echo of the scattered signal that arrives at a slightly later time. There is also the possibility of seeing waves that have reflected off the back edge twice (generator to back edge to weld to back edge to detector), but these arrive far later than the waves of interest. Waves can be reflected from the side of the sample, although this is only a concern at the very start and end of the B-scan, and as mentioned previously, the behaviour of these waves in the B-scan makes them easy to spot.

Despite the presence of some potentially interfering signals, all six defects could be identified, with either 6 mm (higher frequency range of operation) or 10 mm wavelength (lower frequency range of operation) EMATs, and from any inspection side. An example A-scan and B-scan are shown in Fig. 5, and the results are summarised in Figs. 6 and 7; the peaks in the peak-to-peak amplitude represent the presence of a defect. It can be seen that the peaks, in general, extend over the region occupied by the defect, as indicated by the dashed magenta lines. These results were obtained with minimal processing of the B-scan data.

The received signals, $s(t,p)$, where t is time and p is lateral position, have the median of each constant time line in the B-scan, $\tilde{s}(t)$, subtracted from each line (a tilde over a letter represents the median value). Note that the median is not taken along the time dimension of the array, but the lateral position dimension of the array; this way it removes features that are constant over the scan rather than any DC offset for an individual scan:

$$s'(t,p) = s(t,p) - \tilde{s}(t) \tag{1}$$

The modified signal $s'(t,p)$ is brick-wall band-pass filtered in the range 200–900 kHz (this is of course performed along the time dimension of each scan), forming $s'_f(t,p)$. Simple time-gating then extracts the section of interest for measuring the peak-to-peak amplitude for each individual scan, $m(p)$. For the 10 mm wavelength EMATs, the region was 70–120 μs for the in-line configuration, and 80–150 μs for the side-by-side configuration. For the 6 mm wavelength EMATs, the region was 80–150 μs for the in-line configuration, and 90–150 μs for the side-by-side configuration.

$$m(p) = \max(s'_f(t,p)) - \min(s'_f(t,p)) \tag{2}$$

$$70\ \mu s < t_{\text{in-line, } \lambda = 10\ \text{mm}} < 120\ \mu s \tag{3}$$

$$80\ \mu s < t_{\text{side-by-side, } \lambda = 10\ \text{mm}} < 150\ \mu s \tag{4}$$

$$80\ \mu s < t_{\text{in-line, } \lambda = 6\ \text{mm}} < 150\ \mu s \tag{5}$$

$$90\ \mu s < t_{\text{side-by-side, } \lambda = 6\ \text{mm}} < 150\ \mu s \tag{6}$$

Finally, for display purposes, the overall minimum value for the peak-to-peak amplitude is subtracted, so that the lowest value is zero, and this is then divided by its overall maximum value; the useful range of the plot is maximised, making any defects appear more clearly:

$$m'(p) = m(p) - \min(m(p)) \tag{7}$$

$$m''(p) = m'(p)/\max(m'(p)) \tag{8}$$

The results between the different configurations and sides are consistent in their ability to detect the defects, but some defects show up much more clearly from some sides than from others. It is important to note that all the defects can be detected from every side, using both configurations, and using either the 6 mm or 10 mm wavelength EMATs. The in-line configuration is favoured however, as it allows for a slightly larger region to be scanned. It also does not particularly matter in this case if the 10 mm or 6 mm wavelength EMATs are used. Research into gaining additional information about the defect from the received signal, such as defect type identification, would require a sample with a better isolated (cleaner) signal, as this sample has too many interfering signals for it to be unambiguously said that a signal is only due to a single defect.

4. Inspection using a phased array

The phased array scan configuration is shown in Fig. 8. An Olympus 5L64-A12 probe was used, with 64 elements at a pitch of 0.60 mm (total active length of 38.4 mm), and a specified 5.0 MHz centre frequency (5.17 MHz reported in the calibration document). This was attached to an Olympus SA12-N60L wedge (60° LW nominal refracted beam angle in steel). Other options available

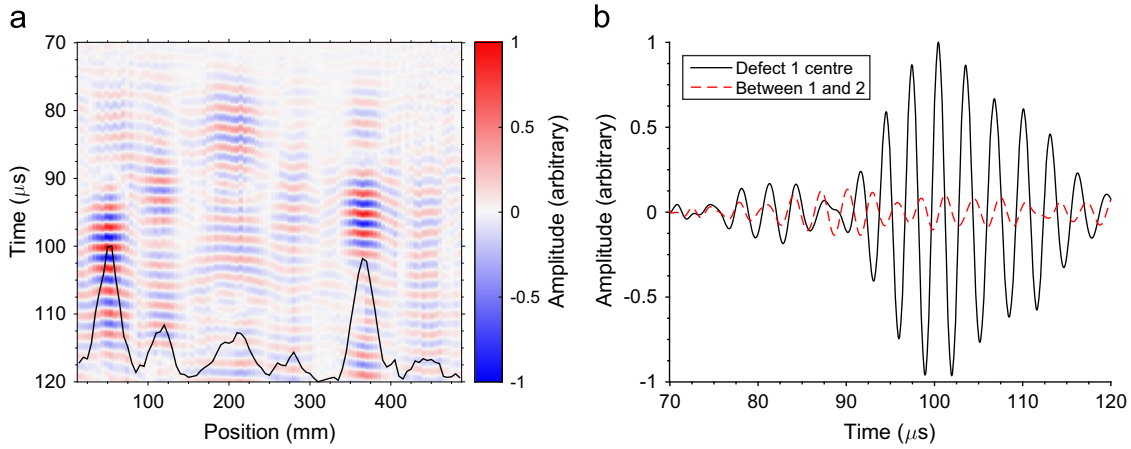

Fig. 5. These are A/B-scans of the weld in the thick stainless steel plate, using 10 mm wavelength SH EMATs in an in-line configuration, from the side labelled TA (see Fig. 4). The B-scan (a) has the peak-to-peak amplitude superimposed upon it (the black line). The A-scans (b) are for the centre of defect 1 (a position of 55 mm), represented by the black solid line, and between defects 1 and 2 (a position of 85 mm), represented by the red dashed line. As the defects occupy a large amount of the length of the weld, the B-scan can be difficult to interpret without calculating the peak-to-peak amplitude. (For interpretation of the references to color in this figure caption, the reader is referred to the web version of this paper.)

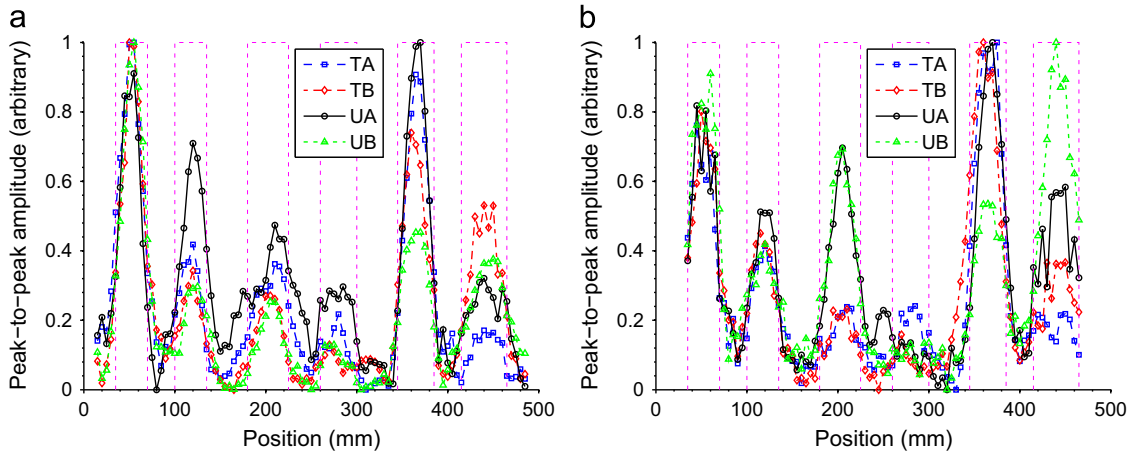

Fig. 6. These are scans of the weld in the thick stainless steel plate, using 10 mm wavelength SH EMATs. The two figures are for each of the two possible configurations, in-line (a) and side-by-side (b), as described in Fig. 4. The magenta dashed lines represent the defect positions. (For interpretation of the references to color in this figure caption, the reader is referred to the web version of this paper.)

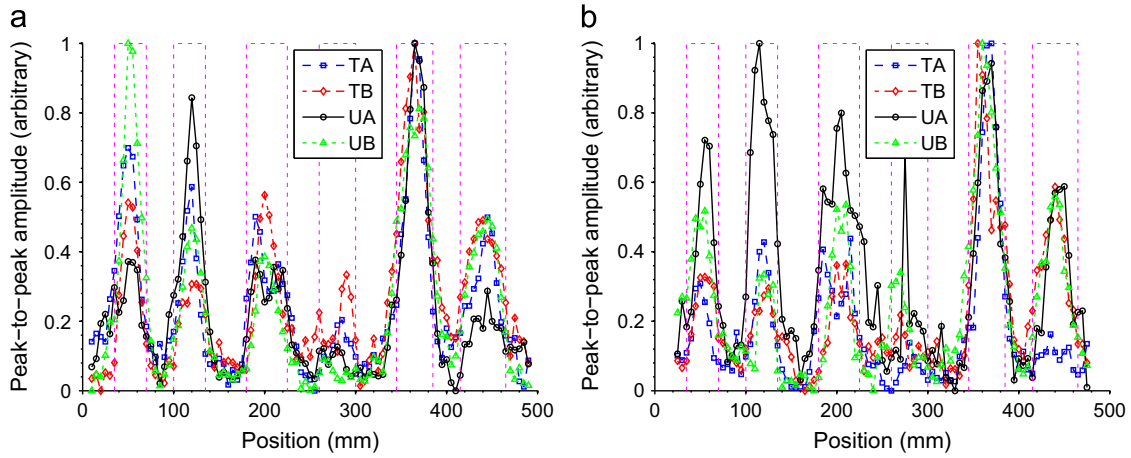

Fig. 7. These are scans of the weld in the thick stainless steel plate, using 6 mm wavelength SH EMATs. The two figures are for each of the two possible configurations, in-line (a) and side-by-side (b), as described in Fig. 4. The magenta dashed lines represent the defect positions. (For interpretation of the references to color in this figure caption, the reader is referred to the web version of this paper.)

from Olympus were also tested, such as the 5L64-A12 with a SA12-N55S wedge (55° SW), a 2.25L32-A5 probe (32 elements, 0.75 mm pitch, 2.25 MHz centre frequency) with a SA5-N60L wedge (60° LW), and a 1.5L16-A4 probe (16 elements, 2.80 mm pitch, 1.5 MHz centre frequency) with a SA4-N45L wedge (45° LW). However, for this particular inspection, the 5L64-A12 probe with

SA12-N60L wedge provided the best results, and the other options, although tested to the same extent, are not considered further in this paper. As for the EMAT configuration, the scan proceeds laterally across the sample (parallel to the weld), with the direction chosen so that for each side of the weld/plate, the scan starts at the same section of weld. As before, the scan progresses in 5 mm increments, and the lateral scan position relates to the lateral centre of the transducer. At each scan position, each transducer was pulsed four times so that the received data was the result of averaging four collections; all averaging was done after the data was transferred to the MATLAB control software on the computer.

The phased array was controlled by a Peak NDT MicroPulse 5. With 128 parallel phased array channels (for generation and detection), this unit allows for great flexibility in how elements are pulsed and how data is received, and in this case it was configured for FMC (using custom MATLAB code rather than the provided software, as this allowed for greater control). The sampling frequency was set at 50 MHz, and 3000 time points were collected for each receiver during every collection; a band-pass filter was applied by the MicroPulse with cut-off points 0.75 MHz and 20.0 MHz. The pulse width when emitting was set at 200 ns (one period of a 5 MHz wave).

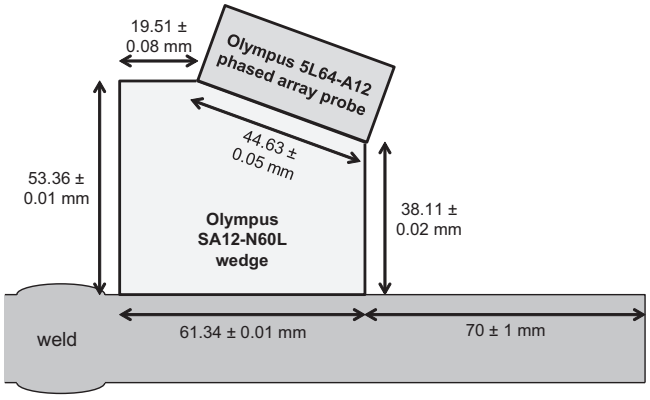

Fig. 8. This is the phased array scan configuration for the thick stainless steel plate with a weld. The back edge of the wedge is 70 mm from the back edge of the plate, and the weld cap starts at approximately 135 mm from the back edge (with some variations between sides). Although not labelled in this diagram, the sides are the same (TA, TB, UA, and UB) as for Fig. 4.

Before the TFM process is applied, the data is brick-wall band-pass filtered in MATLAB, with cut-offs at 0.5 MHz and 10.0 MHz. For the imaging process to work, values for compression wave speeds in the wedge and the steel are required, and both were measured using a simple pulse-echo technique. The depth of the steel plate and the width of the wedge (the dimension between the two large flat sides) were measured using vernier callipers, and the phased array probe placed such that the waves propagated directly through the thickness measured, and reflected from the back-wall (where the back-wall is parallel to the surface the probe is placed on). A simple speed measurement is possible by comparing the time between multiple echoes (the first echo alone cannot be used due to the need to pick a consistent point on the received wave for comparison). The compression wave speeds in the wedge and steel plate are 2330 m/s and 5740 m/s respectively. This speed measurement process has an additional benefit; when measuring the speed, a point within the centre of the reflected waveforms is chosen as the consistent measurement point. As discussed, the time between these points is unlikely to be exactly equal to the time the digitiser starts recording (the zero time) to the same centre point of the first reflection. By subtracting the time of the first centre point from the difference in arrival time between multiple reflections, the effective first time point is obtained. In this case, the first time point is -700 ns (meaning that the time from when the digitiser starts recording to the centre of the first reflection is 700 ns longer than the time between multiple reflections). The advantage is that any flight times will then correspond to the centre of any waveform received from that scattering point. Unfortunately, the speed measured in the steel will not be accurate within the weld and potentially the HAZ, and this will reduce the accuracy with which a defect position can be ascertained (the position will potentially be offset and smeared out), but it should not prevent detection of a defect.

The results of the TFM process are shown in Fig. 9. A clear defect can be seen in Fig. 9a, but it seems to appear outside of the weld region, and indeed, outside the plate, since the plate is 22 mm thick and the weld extends to approximately 90 mm on the X position. This is actually because the path of the wave is not directly from the wedge to the defect, it has reflected off the back-wall and front surface of the plate before reaching the defect, and it has also been reflected in a similar way on the return journey

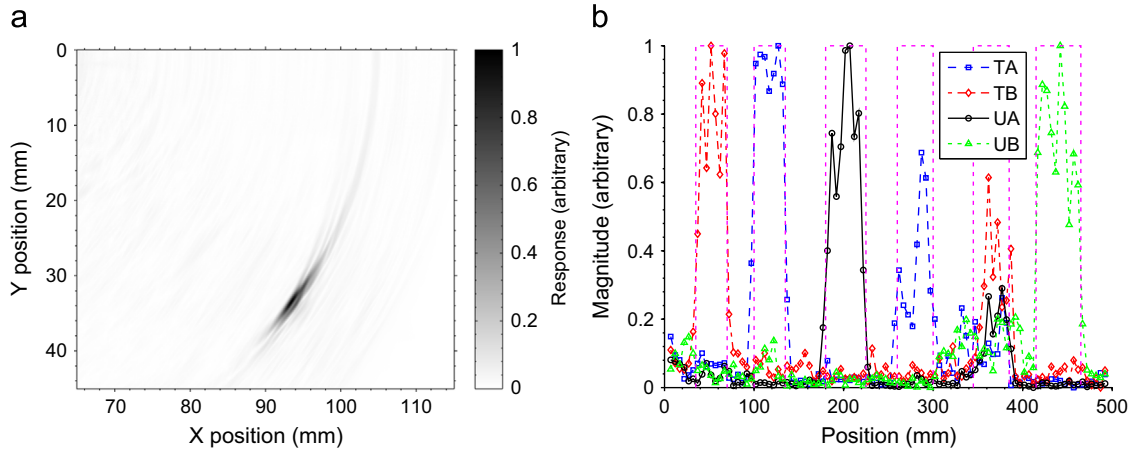

Fig. 9. These are scans of the weld in the thick stainless steel plate, using a 64 element phased array probe attached to a wedge and FMC/TFM (the presence of the wedge is incorporated into the TFM processing). An example output of the TFM algorithm is shown (a) for underside B (UB) at a lateral position of 442 mm. The *X* position axis is relative to the back of the wedge, with the weld starting at 65 mm (just under 4 mm from the front of the wedge). The *Y* position is relative to the plate surface, extending into its thickness. A summary of the TFM results for every side and lateral scan position (b) is taken by finding the maximum response from each TFM image for each scan. In both (a) and (b) the response is scaled such that one is the maximum response for that side, and zero is the minimum (background) response for that side. The magenta dashed lines in (b) represent the defect positions. (For interpretation of the references to color in this figure caption, the reader is referred to the web version of this paper.)

Table 2
The SH PPM EMAT inspection successfully located all the defects from every side of the plate/weld. This table shows the defects found using the phased array generating and detecting compression waves (using FMC/TFM), with a √ representing a success in finding that defect from that position. The sides are labelled as in Fig. 4. The phased array could only detect two defects from each side on average.

Side	Defect					
	1	**2**	**3**	**4**	**5**	**6**
Top side A (TA)		√		√	√	
Top side B (TB)	√				√	
Underside A (UA)			√		√	
Underside B (UB)					√	√

back to the probe. This has been incorporated into the TFM imaging by simply extending the imaging region, which is a valid approach if the two surfaces of the plate are parallel, and the reflections specular. The defect will be within the weld region, and the exact position could be obtained from the TFM image. However, for a comparison with the SH wave experiment, it is not necessary to find the exact location within the weld (other than laterally), but it is important to know that the information is available if required, unlike for the SH wave inspection, which can currently only provide the lateral location along the weld (although more positional information may be obtained from further work analysing the time domain signal in greater detail).

As for the inspection with SH waves generated and detected by PPM EMATs, all defects appear in the summary plot of Fig. 9b. However, as is clear from Fig. 6a, the SH wave inspection was able to find every defect from every side of the plate, whereas the phased array inspection was not, and this is summarised in Table 2. An additional advantage of the SH wave inspection is that the transducers can be much further from the weld than the phased array probe, which must be very close, in part due to the high attenuation of steel, but also because the multiple reflections will lead to complicated signals after more than a couple of skips.

5. Conclusions

SH waves generated and detected by PPM EMATs are effective at detecting weld defects, and the extent of indications in the B-scan is a good approximation to the lateral extent of the weld defects. The scan is not particularly sensitive to the wavelength or positional configuration of the EMATs in these experiments, but the 10 mm wavelength EMATs in the in-line configuration provided the best performance by a small margin. All defects in the weld could be detected, regardless of which side of the plate/weld the scan was performed from. In contrast, a scan performed with a phased array using FMC/TFM could detect all the defects, but on average only two from each side of the plate/weld. In addition, the phased array required close proximity to the weld region, since the compression waves rapidly lose energy both due to attenuation (the skips mean that the distance travelled by the wave increases rapidly with the transducer-weld separation), and due to mode-conversion at each reflection from the sample surfaces. An advantage of using SH waves is therefore the ability to inspect from a greater distance, and more importantly, that the inspection can be performed with access to only one side of the plate/weld. An advantage of the phased array however, is that it can provide the position of the defect within the weld, and coupled with the lateral position obtained by scanning, the full 3D position of the defect could be provided. Although not shown here, the different defect indications arrive at different times within the SH EMAT inspection B-scan, and this information could be used to provide some additional positional information. However, as it currently stands, if full positional information was required, the SH EMAT inspection could be used to detect all defects in a weld, and a phased array technique could be used to provide additional information on those it could detect (which may not be all the defects, as shown within this work).

Acknowledgements

This work was supported by the Engineering and Physical Sciences Research Council (EPSRC), grant EP/I03160X/1, through the Research Centre in Non-destructive Evaluation (RCNDE). The authors are very grateful to the project partners, Rolls-Royce and National Nuclear Laboratory (NNL), for providing additional funding, and to AMEC, for supplying the sample. Please contact S. Dixon if access is required to the data used in this article.

References

[1] Weman K. Welding processes handbook. Cambridge, UK: Woodhead Publishing; 2003.
[2] Scruby CB, Drain LE. Laser ultrasonics: techniques and applications. Bristol, UK: Adam Hilger; 1990.
[3] Taylor JL. Basic metallurgy for non-destructive testing. 2nd ed. Northampton, UK: The British Institute of Non-Destructive Testing; 1996.
[4] Charlesworth JP, Temple JAG. Engineering applications of ultrasonic time-of-flight diffraction. Ultrasonic inspection in engineering. 2nd ed. Baldock, UK: Research Studies Press; 2001.
[5] Silk MG, Lidington BH. The potential of scattered or diffracted ultrasound in the determination of crack depth. Non-Destr Test 1975;8(3):146–51.
[6] Silk MG, Lidington BH. Defect sizing using an ultrasonic time delay approach. Br J Non-Destr Test 1975;17(2):33–6.
[7] Lidington BH, Silk MG, Montgomery P, Hammond G. Ultrasonic measurements of the depth of fatigue cracks. Br J Non-Destr Test 18;1976:165–70.
[8] Dixon S, Edwards C, Palmer SB. A laser-EMAT system for ultrasonic weld inspection. Ultrasonics 1999;37(4):273–81.
[9] Mi B, Ume C. Real-time weld penetration depth monitoring with laser ultrasonic sensing system. J Manuf Sci Eng—Trans ASME 2006;128(1):280–6.
[10] Ogilvy JA. Ultrasonic beam profiles and beam propagation in an austenitic weld using a theoretical ray tracing model. Ultrasonics 1986;24(6):337–47.
[11] Graff KF. Wave motion in elastic solids. New York, USA: Dover Publications; 1975.
[12] Rose JL. Ultrasonic waves in solid media. Cambridge, UK: Cambridge University Press; 1999.
[13] Dixon S, Petcher P, Fan Y, Maisey D, Nickolds P. Ultrasonic metal sheet thickness measurement without prior wave speed calibration. J Phys D: Appl Phys 2013;46(44):445502.
[14] Fortunko CM, Moulder JC. Ultrasonic inspection of stainless steel butt welds using horizontally polarized shear waves. Ultrasonics 1982;20(3):113–7.
[15] Vasile CF, Thompson RB. Excitation of horizontally polarized shear elastic waves by electromagnetic transducers with periodic permanent magnets. J Appl Phys 1979;50(4):2583–8.
[16] Hirao M, Ogi H. An SH-wave EMAT technique for gas pipeline inspection. NDT & E Int 1999;32(3):127–32.
[17] Ogi H, Goda E, Hirao M. Increase of efficiency of magnetostriction SH-wave electromagnetic acoustic transducer by angled bias field: piezomagnetic theory and measurement. Jpn J Appl Phys Part 1—Regul Pap Short Notes Rev Pap 2003;42(5):3020–4.
[18] Grubin HL. Direct electromagnetic generation of compressional waves in metals in static magnetic fields. IEEE Trans Sonics Ultrasonics 1970;17(4):227–9.
[19] Kawashima K. Theory and numerical calculation of the acoustic field produced in metal by an electromagnetic ultrasonic transducer. J Acoust Soc Am 1976;60(5):1089–99.
[20] Thompson RB. Physical principles of measurements with EMAT transducers. Ultrasonic measurement methods. Physical acoustics, vol. XIX. London, UK: Academic Press; 1990. p. 157–200.
[21] Kawashima K, Wright OB, Hyoguchi T. High frequency resonant electromagnetic generation and detection of ultrasonic waves. Jpn J Appl Phys Part 1—Regul Pap Short Notes Rev Pap 1994;33(5):2837–45.
[22] Hirao M, Ogi H. Electromagnetic acoustic resonance and materials characterization. Ultrasonics 1997;35(6):413–21.
[23] Ogi H. Field dependence of coupling efficiency between electromagnetic field and ultrasonic bulk waves. J Appl Phys 1997;82(8):3940–9.
[24] Dixon S, Edwards C, Palmer SB. High accuracy non-contact ultrasonic thickness gauging of aluminium sheet using electromagnetic acoustic transducers. Ultrasonics 2001;39(6):445–53.
[25] Hirao M, Ogi H. EMATs for science and industry: noncontacting ultrasonic measurements. London, UK: Kluwer Academic Publisher; 2003.

[26] Silk MG. Ultrasonic transducers for nondestructive testing. Bristol, UK: Adam Hilger Ltd; 1984.
[27] Ohtsuka Y, Higashib M, Nishikawa M. Fundamental experiment for inspection of cooling pipes in operation by using ultrasonic technique. Fus Eng Des 2006;81(8–14):1583–7.
[28] Moran TJ, Panos RM. Electromagnetic generation of electronically steered ultrasonic bulk waves. J Appl Phys 1976;47(5):2225–7.
[29] Sato M, Okano H, Ishikawa M. Development of ultrasonic testing equipment incorporating electromagnetic acoustic transducer. J Nucl Sci Technol 1992;29 (4):400–7.
[30] Dixon S, Edwards C, Palmer SB. Texture measurements of metal sheets using wideband electromagnetic acoustic transducers. J Phys D: Appl Phys 2002;35 (8):816–24.
[31] Hubschen G, Salzburger HJ. Inspection of dissimilar metal welds using horizontally polarized shear (SH-)waves and electromagnetic ultrasonic (EMUS-)probes. Int J Press Vessels Pip 1989;39(4):331–44.
[32] Sawaragi K, Salzburger HJ, Hubschen G, Enami K, Kirihigashi A, Tachibana N. Improvement of SH-wave EMAT phased array inspection by new eight segment probes. Nucl Eng Des 2000;198(1–2):153–63.
[33] Maclauchlan DT, Clark SP, Hancock JW. Application of large aperture EMATs to weld inspection. In: Review of progress in quantitative nondestructive evaluation: Proceedings of the 34th annual review of progress in quantitative nondestructive evaluation. AIP Conference Proceedings, vol. 975. Golden (Colorado), USA: AIP; 2008. p. 817–22.
[34] Salzburger HJ, Niese F, Dobmann G. EMAT pipe inspection with guided waves. Weld World 2012;56(5–6):35–43.
[35] Gao H, Ali SM, Lopez B. Inspection of austenitic weld with EMATs. In: Review of progress in quantitative nondestructive evaluation: Proceedings of the 36th annual review of progress in quantitative nondestructive evaluation. AIP Conference Proceedings, vol. 1211. Kingston (Rhode Island), USA: AIP; 2010. p. 1175–81.
[36] Holmes C, Drinkwater BW, Wilcox PD. Post-processing of the full matrix of ultrasonic transmit–receive array data for non-destructive evaluation. NDT & E Int 2005;38(8):701–11.
[37] Marple S.L. Computing the discrete-time analytic signal via FFT. IEEE Trans Signal Process 47(9);1999:2600–3.